IEEE Geoscience And Remote Sensing Magazine, Available online 30 November 2022
DOI:10.1109/MGRS.2022.3219778

FSSCat: Demonstrating the Capabilities of CubeSats to Monitor Essential Climate Variables of the Water Cycle

A. Camps[1,2], J.F. Munoz-Martin[1,3], J.A. Ruiz-de-Azua[1,4], L. Fernandez[1], A. Perez-Portero[1], D. Llavería[1], C. Herbert[1], M. Pablos[5], A. Golkar[6,1], A. Gutiérrrez[7], C. António[7], J. Bandeiras[7], J. Andrade[7], D. Cordeiro[7], S. Briatore[8], N. Garzaniti[9,8], F. Nichele[10], R. Mozzillo[10], A. Piumatti[10], M. Cardi[10], M. Esposito[11], C.N. van Dijk[11], N. Vercruyssen[11], J. Barbosa[11], J. Hefele[11], R. Koeleman[11], B. Carnicero Dominguez[12], M. Pastena[12], G. Filippazzo[13], A. Reagan[13]

[1]Universitat Politècnica de Catalunya, Barcelona, Spain
[2]Institut d'Estudis Espacials de Catalunya, Barcelona, Spain
[3]Jet Propulsion Laboratory / California Institute of Technology, Pasadena, USA
[4]i2Cat, The Internet Research Center, Barcelona, Spain
[5]Institut de Ciències del Mar (ICM-CSIC) & Barcelona Expert Center (BEC) on Remote Sensing, Barcelona, Spain
[6]Technical University of Munich, Department of Aerospace and Geodesy Munich, Germany
[7]Deimos Eng., Lisbon, Portugal
[8]Golbriak Space OÜ, Tallin, Estonia
[9]Cranfield University, School of Aerospace, Transport and Manufacturing, UK
[10]Tyvak International, Torino, Italy
[11]Cosine, Oosteinde, The Netherlands
[12]ESA ESTEC, Noordwijk, The Netherlands
[13]ESA ESRIN, Frascati, Italy
E-mail: adriano.jose.camps@upc.edu
Tel: +34 934054153

Abstract—The "Federated Satellite Systems" (FSSCat) mission was the winner of the ESA S^3 Challenge and overall winner of the 2017 Copernicus Masters competition. It consisted of two 6-unit CubeSats. The Earth Observation payloads were: 1) FMPL-2 onboard ^{3}Cat-5/A, an L-band microwave radiometer and GNSS-Reflectometer implemented using a Software Defined Radio, and 2) Hyperscout-2 onboard ^{3}Cat-5/B, a hyperspectral camera with the first experiment using artificial intelligence to discard cloudy images. FSSCat was launched on September 3rd 2020 and injected in a 535 km height Syn synchronous orbit. ^{3}Cat-5/A was operated for 3 months until the payload was probably damaged by a solar flare and a coronal mass ejection. During this time, all scientific requirements were met, including the generation of coarse resolution and downscaled soil moisture maps, sea ice extent, concentration and thickness maps, and even wind speed and sea surface salinity maps, which were not originally foreseen. ^{3}Cat-5/B was operated a few more months until the number of images acquired met the requirements. This manuscript briefly describes the FSSCat mission and the FMPL-2 payload, summarizes the main scientific results.

***Index Terms*—CubeSats, GNSS-Reflectometry, Microwave Radiometry, Sea Ice, Sea Salinity, Software Defined Radio, Soil Moisture.**

I. Introduction

THE "Federated Satellite Systems/3Cat-5" (FSSCat) mission was the winner of the 2017 ESA S^3 (Sentinel Small Satellite) Challenge and overall winner of the Copernicus Masters competition. FSSCat was proposed by the Universitat Politècnica de Catalunya (UPC), and it consisted of two 6-unit CubeSats, which were successfully launched on September the 3rd, 2020 on the Vega SSMS PoC, flight VV16. The two spacecrafts ^{3}Cat-5/A (International designator 2020-061W, NORAD ID 46292), and ^{3}Cat-5/B (International designator 2020-061X, NORAD ID 46293) are in a 97.4° inclination Sun-synchronous orbit, with a perigee of 535 km, and an apogee of 538 km.

The mission primary goals were the generation of: 1) coarse resolution soil moisture maps, and sea ice extent and thickness maps using L-band microwave radiometry and GNSS-Reflectometry, 2) downscaled soil moisture maps by combining passive microwave and multi-spectral optical data, and 3) testing communication techniques for future satellite federations. Secondary goals are the generation of sea surface salinity and wind speed maps.

^{3}Cat-5/A carries the Flexible Microwave Payload–2 (FMPL-2) [1] designed and implemented by the Universitat Politècnica de Catalunya (UPC). FMPL-2 inherits the concept of the PAU instrument combining an L-band microwave radiometer and a GNSS-Reflectometer in a single instrument [2].

^{3}Cat-5/B carries the HyperScout-2 hyperspectral imager with a field of view is 31°×16° field of view [3]. HyperScout-2 includes two channels: channel 1 in the visible and near infrared, with 4000×1850 pixels, and 45 bands from 400 to 1000 nm, with a spectral resolution of 16 nm; and channel 2 in the thermal infrared, with 1024×768 pixels and 3 bands from 8 to 14 μm, with spectral resolutions of 1100 nm in the first two bands, and 6000 nm in the third one. HyperScout-2 has augmented processing performance by using the PhiSat-1 board featuring the new Myriad 2 artificial intelligence chip, which improves the data processing capabilities for hyperspectral imagery [4].

In addition, both CubeSats include an optical inter-satellite link from Gölbriak Space, and a UHF inter-satellite link tech-demos from UPC to test the concept of satellite federations.

Thanks to the background and previous experience of the teams, this challenging mission was implemented in just 1.5 years. In addition to UPC and Gölbriak, Deimos Engenharia (PT) was the prime contractor of the mission and responsible for the Data Processing Ground Segment, Tyvak International (IT) was the platform provider, system integrator, CubeSat deployer and launch interface provider, and the operations manager, and ESA EOP which initiated the ESA Sentinel Small Satellite Challenge, provided technical and programmatic advise and expertise, the funding scheme, and access to ESA testing facilities.

Two weeks after launch, the commissioning phase of ^{3}Cat5/A was declared successful. The FMPL-2 payload was first executed on September 14th, 2020. The payload commissioning lasted 10 days, and it was formally finalized on September 25th, 2020. During these first days, the instrument was successfully executed 8 times over the North Pole, providing quality radiometric measurements at L-band, and GNSS-R measurements that were used to calibrate and tune the configuration of the instrument. Data showed an absolute accuracy of the FMPL-2 radiometer better than ~0.5 K, and the radiometric sensitivity was estimated to be ~0.2 K over the ocean, and ~0.5 K over land, for an integration time of 100 ms [5]. The long-term stability was also estimated in Fig. 10 of [5] as < 0.5 K over 12 days.

Since then, the instrument entered into nominal operations, being executed over the poles following a 5-day basis: 5 days in a row over the North Pole at latitudes >55°, and 5 days in a row over the South Pole at latitudes <-55°. The minimum latitude was decreased to 45° after 1 month of the mission, and finally to 35°, thanks to a positive power budget and the downlink capability of ^{3}Cat-5/A data at the UPC ground station at the Observatori Astronòmic del Montsec (OAdM), owned and operated by the IEEC [6]. FMPL-2 was operated until December 4th, 2020 when, after the three months of operations originally planned, the spacecraft could no longer communicate with the payload, which was probably damaged by the solar flare and Coronal Mass Ejection (CME) occurred on November 29th, 2020, the most powerful ones until then in the Solar Cycle 25 [7].

This paper describes the FMPL-2 payload architecture, and presents its main scientific results obtained during the three months of operation.

II. The FMPL-2 Payload: A Novel SDR-Based Hybrid L-Band Radiometer and GNSS-Reflectometer

FMPL-2 is a combined L-band microwave radiometer and GNSS-Reflectometer implemented using a Zynq-7000 Software Defined Radio (SDR) [1]. L-band microwave radiometry can be used to infer surface soil moisture and sea ice thickness up to ~60 cm [8]. Downscaled soil moisture maps can be generated using validated algorithms developed for ESA SMOS using VNIR data [9].

Figure 2a shows the RF-Front End block diagram of FMPL-2. The upper branch is connected to the right-hand circular polarization (RHCP) up-looking antenna to pick the direct GNSS signal used as a reference (output I1), and is connected to the GNSS receiver. The lower branch is connected to a 6 dual-band left-hand circular polarization (LHCP) down-looking antenna array (Figs. 1b, and 2b) to pick the reflected GNSS signals (GPS and Galileo) at 1575 MHz, and the radiometric signal at 1413 MHz. From 535 km height, he footprint of the down-looking antenna was 350 km x 500 km. The input of the second branch can be selected among the down-looking antenna, and an active cold load (ACL) and a matched load for internal absolute calibration of the microwave radiometer. Since the two receiver inputs of the Zynq-7000 have to be at the same frequency, a transmitter output is used as a local oscillator of the I2 branch. An integration time of 100 ms was selected for the microwave radiometer, as the radiometric sensitivity (~0.2 K) was enough to compensate for the wind speed effects of the brightness temperatures (BT) over the ocean. This custom-made RF-Front End (Fig. 2c) was manufactured by Balamis SL, and UPC spin-off company.

A GNSS-Reflectometer can be understood as a multi-static radar with as many transmitters as navigation satellites are in view, and raw data can be typically processed as a scatterometer, but it can also be processed as an altimeter, or even as an unfocused synthetic aperture radar (SAR). The most general GNSS-R observable is the so-called Delay-Doppler Map (DDM), which in the so called "conventional GNSS-R" is computed from the complex cross-correlation of the reflected GNSS signal with a locally-generated replica of the transmitted GNSS signal for different Doppler frequencies, and delay bins [10]. GNSS-R is very sensitive to the parameters of the surface where the scattering is taking place, and the peak and shape of the DDM contain information on the reflectivity itself, and the mean squared slopes of the surface where the scattering is taking place. Over the ocean the DDM is much more spread, both in the delay and Doppler frequency domains, than it is over sea ice or land [10], and this spread can be related to e.g. the wind speed (e.g. [11-13]), although it is affected by swell, rain and other effects.

To optimize the spatial resolution for sea ice extent detection, the GNSS-R incoherent integration time was set to 40 ms, so that the blurring induced by the subsatellite point movement is about the size of the first Fresnel zone (~300 m), i.e. the spatial resolution under coherent scattering conditions [14,15].

III. Scientific Data Processing

Five scientific products have been obtained using Artificial Neural Networks (ANN) that have been trained using different input variables for each product, and "ground truth" as the output.

A. Soil Moisture

Soil Moisture (SM) was retrieved using a 2-hidden layer feed-forward ANN with 7 neurons in each layer. The input variables are: the land surface temperature (ERA 5 skin temperature from ECMWF, with a 30 km resolution), the red and near-infrared bands of multispectral images or directly the NDVI from e.g. NASA MODIS, at 9 and 36 km spatial resolution obtained aggregating to original 1 km spatial resolution product, and the FMPL-2 LHCP L-band BTs from the nadir-looking antenna. The ANN was trained with 60% of the data to avoid overfitting, using the 36 km SMAP soil moisture product, and the training was interrupted after 20 epochs.

Figure 3a shows a sample soil moisture map produced over a week. Figure 3b shows the scatter plot of the soil SMAP moisture values, and the FMPL-2/ANN retrieved ones. The R^2 coefficient is 0.8, and the standard deviation of the error with respect to the SMAP product is 9.2%, which is ~2-2.5 times larger than the ~4% accuracy quoted for SMOS soil moisture products. The interested reader is referred to [16] for further details.

B. Sea Ice Concentration/Extent

Sea ice concentration (SIC) maps were generated using L-band microwave radiometry and/or GNSS-R data. Two regression fit ANNs were used for each data with 3 hidden layers of 5, 10 and 5 neurons each, and 5 and 8 input variables, respectively. The L-band microwave radiometry ANN was trained using OSI SAF [17] sea ice cover, or NSIDC ground truth as a target output, and FMPL-2 BTs, the along-track standard deviation and gradient of the BTs, the ERA 5 skin temperature from ECMWF, and the land cover fraction (%) are used as input variables. For GNSS-R the inputs are the FMPL-2 BTs, the averaged DDM, the reflectivity, the standard deviation of the reflectivity, the DDM signal-to-noise ratio, the elevation angle of the reflected signal, the land cover fraction within an area larger than the antenna footprint, and the ERA 5 skin temperature. All variables were bilinearly interpolated to the GNSS-R specular reflection points, and the FMPL-2 BTs were needed to improve the performance of the network. Both networks were trained using ~15.000 random samples for each pole, and they were validated using ~5.000 random samples for each pole.

Sea Ice Extent (SIE) maps were generated using a binary classification ANN with only one hidden layer with 10 neurons. Figure 4 shows sample SIE (top) and SIC (center) maps for the Arctic (left) and Antarctica (right) derived from the FMPL-2. The performance of these ANNs is summarized in Table I. As it can be seen in Figs. 4a and 4b, although the GNSS-R reflectivity is only available over the specular reflection points, its variations offer a finer granularity of the sea ice extent that is not captured by the microwave radiometry data. Figure 4c shows the temporal evolution of the SIE during October and November. Note that, as compared to OSI SAF "ground truth", the error is smaller than 6% which is comparable to the errors between different SIE products. The interested reader is referred to [18] for further details.

C. Sea Ice Thickness

Sea Ice Thickness (SIT) maps are generated using a predictive regression model - Deep Neural Network (DNN) with a normalization layer, two hidden dense non-linear layers with 64 neurons each, and one linear single output layer. The input variables are the FMPL-2 BTs, the ERA 5 skin temperature from ECMWF, and the OSI SAF OSI-401-b SIC product. Since the only sea ice thickness "ground truth" data available is the one generated by the SMOS mission, this is the training output variable used.

Figure 5 presents some results for the a) Arctic, and b) Antarctica. Figure 5c shows the scatter plot of the SMOS-derived SIT used as a ground truth, and the FMPL-2/DNN-derived SIT. A good agreement is found up to ~50 cm SIT. Beyond ~50 cm the sea ice is too thick to "see" the sea water, and be able to quantify the ice thickness impact in the BTs. Figure 5d shows the Mean Absolute Error (MAE) histogram, showing a nearly unbiased SIT prediction with a standard deviation of just 6.5 cm, just slightly larger than the SMOS one. The interested reader is referred to [19] for further details.

D. Wind Speed

Wind speed (WS) is a proxy for the sea state roughness, and it has to be precisely estimated in order to retrieve the sea surface salinity (SSS). To do that, the correlation with other geophysical variables was first studied. As expected, the GNSS-R data present a very small correlation with respect to the Sea Surface Temperature (SST), and a negative correlation (~ -0.25) with respect to the WS, and also the SSS, although this last correlation may be also influenced by geographical effects (i.e. higher wind speeds at higher latitudes, with lower SSS). A slightly larger correlation (~ -0.3) was also found between the moving standard deviation of the reflectivity (Γ) and the WS product. Finally, the L-band BTs exhibited a small correlation with respect to the WS, the SST, and the SSS.

When trying to retrieve the WS from FMPL-2 data, several ANNs were tested. The training process followed the same approach as for others: data was randomly split into 20% for training, and 80% for testing. It was found that, for low wind speeds, GNSS-R data perform better than the L-band BTs, and vice-versa. Therefore, the WS estimate was significantly better when combining both GNSS-R and L-band BTs. However, the best results were obtained with an ANN that included the SST and the SSS data, as well. In this case, the correlation coefficient increased up to $R^2 = 0.89$, and the RMSE reduced down to 1.68 m/s. The interested reader is referred to [20] for further details.

E. Sea Surface Salinity

SSS maps are generated using an ANN topology with two hidden layers, with 8 neurons each. SSS can be derived from L-band microwave radiometry data, but the SSS signature is easily hidden by the sea surface roughness effects. Therefore, the best SSS results were achieved when combining L-band BTs, SST, and GNSS-R data (reflectivity, moving standard deviation of the reflectivity, and elevation angle of the reflected signal, as a proxy for sea surface roughness). The ANN is trained using 20% of the available points and the SMOS SSS maps, as they are the only existing ones, and the other 80% was used for testing. Figure 6 shows sample results of the SSS retrieved, ground truth, and error maps over a) the Arctic, b) Antarctica, and error statistics: c) SMOS SSS ground truth - FMPL-2 ANN SSS scatter plot, and d) MAE histogram. In one overpass the SSS RMSE is 0.43 psu, while SMOS SSS maps have a nominal error of 0.1 psu every 100 km × 100 km, and every month. Assuming that errors follow a normal distribution and are uncorrelated, the RMSE averages with the square root of the number of data averaged, so homogenizing the revisit times and spatial resolutions the FMPL-2 SSS RMSE averaged over a month would be ~0.43 psu/$\sqrt{30} \approx 0.08$ psu, while SMOS SSS RMSE over a 350 km × 500 km pixel would be 0.1 psu//$\sqrt{(3.5 \times 5)} \approx 0.024$ psu, that is FMPL-2 SSS RMSE is ~ 4 times larger than that of SMOS. The interested reader is referred to [20] for further details.

IV. Conclusion

The FSSCat mission and the main scientific results of the FMPL-2 combined microwave radiometer and GNSS-R payload onboard the 3Cat-5/A spacecraft have been presented. A number of climate variables associated to the water cycle have been presented: soil moisture, downscaled using visible and near-infrared data, sea ice concentration, extent and thickness, sea surface wind speed, and sea salinity.

FSSCat is the first ESA Third Party Mission based on CubeSats [21], and all data is freely available at: https://catalogue.nextgeoss.eu/.

The mission was implemented in a record time (1.5 year), although its launch was delayed one more year due to Vega 15 explosion, and the COVID-19 lock down of the Kourou spaceport.

FSSCat has shown the potential of small satellites to conduct valuable science missions, either as gap-fillers between high-end missions, or simply to reduce the revisit time by forming satellite constellations with a slightly worse performance than full-fledged missions, but at a fraction of their cost (e.g. 3Cat-5/A with FMPL-2 cost is ~1.5 M$, including launch, SMOS is ~315M$, and SMAP ~915 M$).

Because of the mass, volume and power limitations, the achievable performance cannot match that of full-fledged high-end missions, but data accuracy can be improved by cross-calibration with data from coetaneous large high-end satellites. For example, a CubeSat based constellation of 8 satellites embarking an FMPL-2 like payload would allow to entirely cover daily all latitudes above +45° N, with enough footprint oversampling to retrieve SM products daily [16], while the revisit time of SMOS is ~3 days at the equator.

3Cat-5/B also implemented the first AI processor in space [3, 4] to download only the cloud-free imagery. It is foreseen that constellations of intelligent Earth Observation sensors, acquiring and downloading only the useful data, and inter-connected satellites, to share resources and reduce latency, will be able to provide global near real-time data for the upcoming digital twins of the Earth.

Acknowledgment

This work was supported by 2017 ESA S3 challenge and Copernicus Masters overall winner award ("FSSCat" project) and ESA project "FSSCat Validation Experiment in MOSAIC", by the Spanish Ministry of Science, Innovation and Universities, "Sensing with Pioneering Opportunistic Techniques" SPOT, grant RTI2018-099008-BC21/AEI/10.13039/501100011033, and by the Unidad de Excelencia Maria de Maeztu MDM-2016-0600.

References

[1] J. F. Munoz-Martin, L. F. Capon, J. A. Ruiz-de-Azua and A. Camps, "The Flexible Microwave Payload-2: A SDR-Based GNSS-Reflectometer and L-Band Radiometer for CubeSats," in IEEE Journal of Selected Topics in Applied Earth Observations and Remote Sensing, vol. 13, pp. 1298-1311, 2020, https://doi.org/10.1109/JSTARS.2020.2977959

[2] A. Camps, X. Bosch-Lluis, I. Ramos-Perez, J. F. Marchan-Hernandez, B. Izquierdo and N. Rodriguez-Alvarez, "New Instrument Concepts for Ocean Sensing: Analysis of the PAU-Radiometer," in IEEE Transactions on Geoscience and Remote Sensing, vol. 45, no. 10, pp. 3180-3192, Oct. 2007, https://doi.org/10.1109/TGRS.2007.894925

[3] HyperScout-2: https://www.cosine.nl/cases/hyperscout-2/ (last visited September 11, 2022)

[4] G. Giuffrida et al., "The Φ-Sat-1 Mission: The First On-Board Deep Neural Network Demonstrator for Satellite Earth Observation," in IEEE Transactions on Geoscience and Remote Sensing, vol. 60, pp. 1-14, 2022, Art no. 5517414, https://doi.org/10.1109/TGRS.2021.3125567

[5] J.F. Munoz-Martin, L. Fernandez, A. Perez, J.A. Ruiz-de-Azua, H. Park, A. Camps, B. C. Domínguez, M. Pastena, In-Orbit Validation of the FMPL-2 Instrument—The GNSS-R and L-Band Microwave Radiometer Payload of the FSSCat Mission. Remote Sens. 2021, 13, 121. https://doi.org/10.3390/rs13010121

[6] UPC NanoSatLab web site: https://nanosatlab.upc.edu/en/facilitiesfolder/ground-segment (last visited September 11, 2022)

[7] Powerful Solar Flare, Coronal Mass Ejection Occur on November 29: https://www.arrl.org/news/powerful-solar-flare-coronal-mass-ejection-occur-on-november-29 (last visited September 11, 2022)

[8] L. Kaleschke, et al., "SMOS sea ice product: operational application and validation in the Barents Sea marginal ice zone". Remote Sensing of Environment 180. (2016): S. 264-273.

[9] G. Portal et al., "A Spatially Consistent Downscaling Approach for SMOS Using an Adaptive Moving Window," in IEEE Journal of Selected Topics in Applied Earth Observations and Remote Sensing, vol. 11, no. 6, pp. 1883-1894, June 2018, https://doi.org/10.1109/JSTARS.2018.2832447

[10] V. U. Zavorotny, S. Gleason, E. Cardellach and A. Camps, "Tutorial on Remote Sensing Using GNSS Bistatic Radar of Opportunity," in IEEE Geoscience and Remote Sensing Magazine, vol. 2, no. 4, pp. 8-45, Dec. 2014, https://doi.org/10.1109/MGRS.2014.2374220

[11] J.L. Garrison, A. Komjathy, V. U. Zavorotny, and S. J. Katzberg. 2002. "Wind Speed Measurement Using Forward Scattered GPS Signals." IEEE Transactions on Geoscience & Remote Sensing 40 (1): 50–65. https://doi.org/10.1109/36.981349

[12] G. Foti, C. Gommenginger, P. Jales, M Unwin, and J. Roselló. "Spaceborne GNSS-Reflectometry for Ocean Winds: First Results from the UK TechDemoSat-1 Mission: Spaceborne GNSS-R: First TDS-1 Results." Geophysical Research Letters 42 (13): 5435–5441, 2015. https://doi.org/10.1002/2015GL064204

[13] M. P. Clarizia and C. S. Ruf, "Wind Speed Retrieval Algorithm for the Cyclone Global Navigation Satellite System (CYGNSS) Mission," in IEEE Transactions on Geoscience and Remote Sensing, vol. 54, no. 8, pp. 4419-4432, Aug. 2016, https://doi.org/10.1109/TGRS.2016.2541343

[14] A. Camps, "Spatial Resolution in GNSS-R Under Coherent Scattering," in IEEE Geoscience and Remote Sensing Letters, vol. 17, no. 1, pp. 32-36, Jan. 2020, https://doi.org/10.1109/LGRS.2019.2916164

[15] A. Camps, and J.F. Munoz-Martin, "Analytical Computation of the Spatial Resolution in GNSS-R and Experimental Validation at L1 and L5," Remote Sens. 2020, 12, 3910. https://doi.org/10.3390/rs12233910

[16] J.F. Munoz-Martin, D. Llaveria, C. Herbert, M. Pablos, H. Park, A. Camps, "Soil Moisture Estimation Synergy Using GNSS-R and L-Band Microwave Radiometry Data from FSSCat/FMPL-2." Remote Sens. 2021, 13, 994. https://doi.org/10.3390/rs13050994

[17] OSI SAF Sea Ice Concentration (SSMIS): https://osi-saf.eumetsat.int/ (last visited September 11, 2022)

[18] D. Llaveria, J.F. Munoz-Martin, C. Herbert, M. Pablos, H. Park, A. Camps, "Sea Ice Concentration and Sea Ice Extent Mapping with L-Band Microwave Radiometry and GNSS-R Data from the FFSCat Mission Using Neural Networks." Remote Sens. 2021, 13, 1139. https://doi.org/10.3390/rs13061139

[19] C. Herbert, J.F. Munoz-Martin, D. Llaveria, M. Pablos, A. Camps, "Sea Ice Thickness Estimation Based on Regression Neural Networks Using L-Band Microwave Radiometry Data from the FSSCat Mission." Remote Sens. 2021, 13, 1366. https://doi.org/10.3390/rs13071366

[20] J.F. Munoz-Martin, A. Camps, "Sea Surface Salinity and Wind Speed Retrievals Using GNSSR and L-Band Microwave Radiometry Data from FMPL-2 Onboard the FSSCat Mission." Remote Sens. 2021, 13, 3224. https://doi.org/10.3390/rs13163224

[21] Introducing the Newest ESA Third Party Missions: https://earth.esa.int/eogateway/news/introducing-the-newest-esa-third-party-missions (last visited September 11, 2022)

TABLE I

Summary of the performance of the sea ice concentration (SIC) and extent (SIE) ANNs

Errors wrt to OSI SAF products.		Arctic		Antarctic	
		SIC	SIE	SIC	SIE
MWR error	Global	2.37%	1.95%	5.55%	3.57%
	Ice areas (SIC > 90%)	2.87%	0.02%	5.25%	0.21%
	Water areas (SIC = 0%)	1.05%	1.52%	2.35%	2.90%
	Transition areas (0 < SIC < 90%)	11.27%	8.50%	11.30%	7.33%
GNSS-R error		2.80%	1.10%	2.29%	1.00%

a) 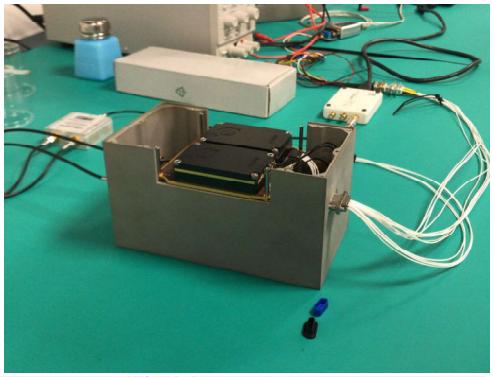

b) 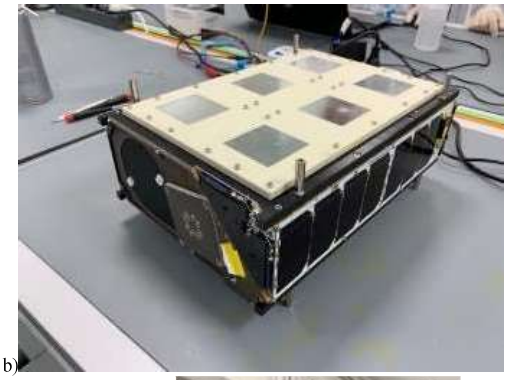

c) 

d) 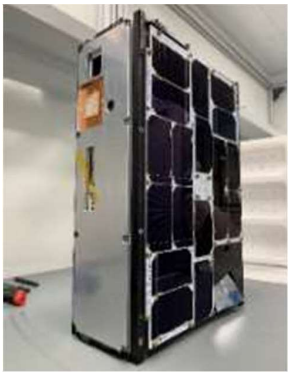

Fig. 1. a) FMPL-2 combined microwave radiometer and GNSS-reflectometer, b) 3Cat-5/A and dual-band nadir looking antenna, c) HyperScout-2, and d) Cat-5/B with HyperScout-2 baffle on the bottom right corner.

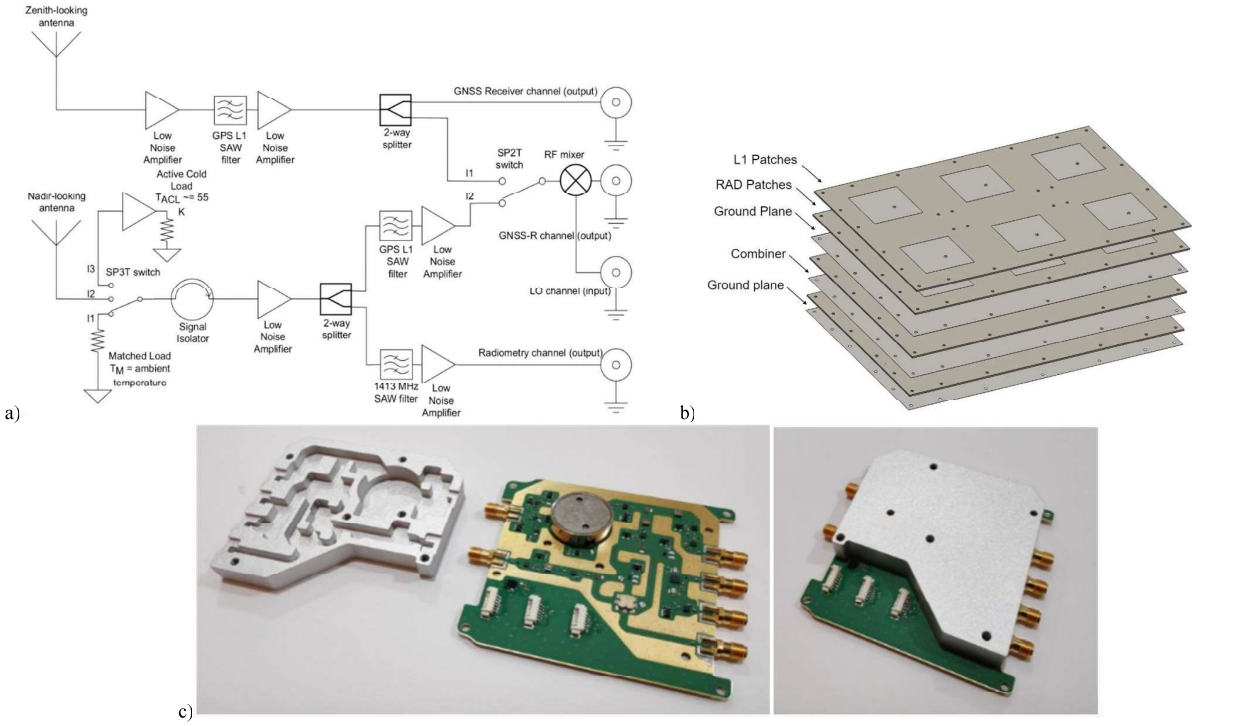

Fig. 2. FMPL-2 payload RF front-end. First connector on the right-hand side goes to a navigation receiver, the second one is an input of a Software Defined Radio (Rx #1), the third one is a transmitter channel (Tx #1) used as local oscillator, and the fourth one is the second input of the Software Defined Radio (Rx #2) (adapted from [1]).

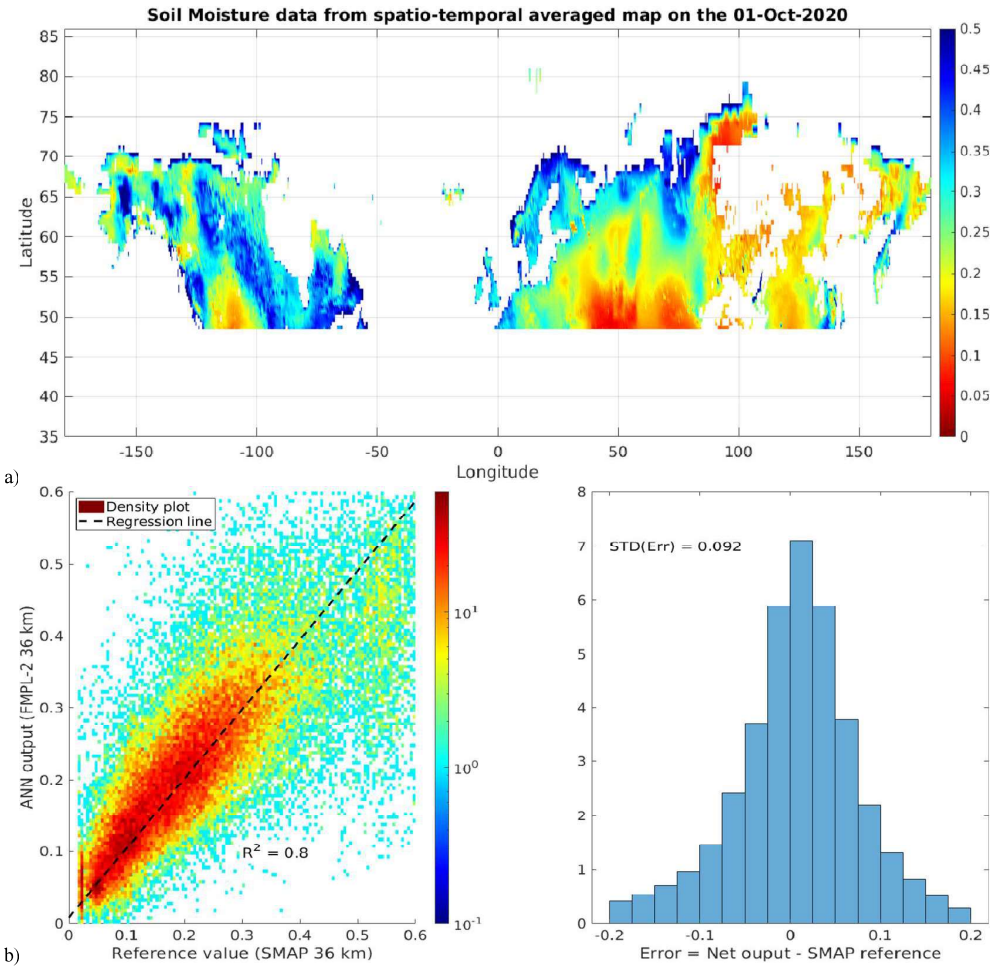

Fig. 3. a) Weekly average soil moisture map derived from FMPL-2 using an ANN, and b) error statistics (from [16]).

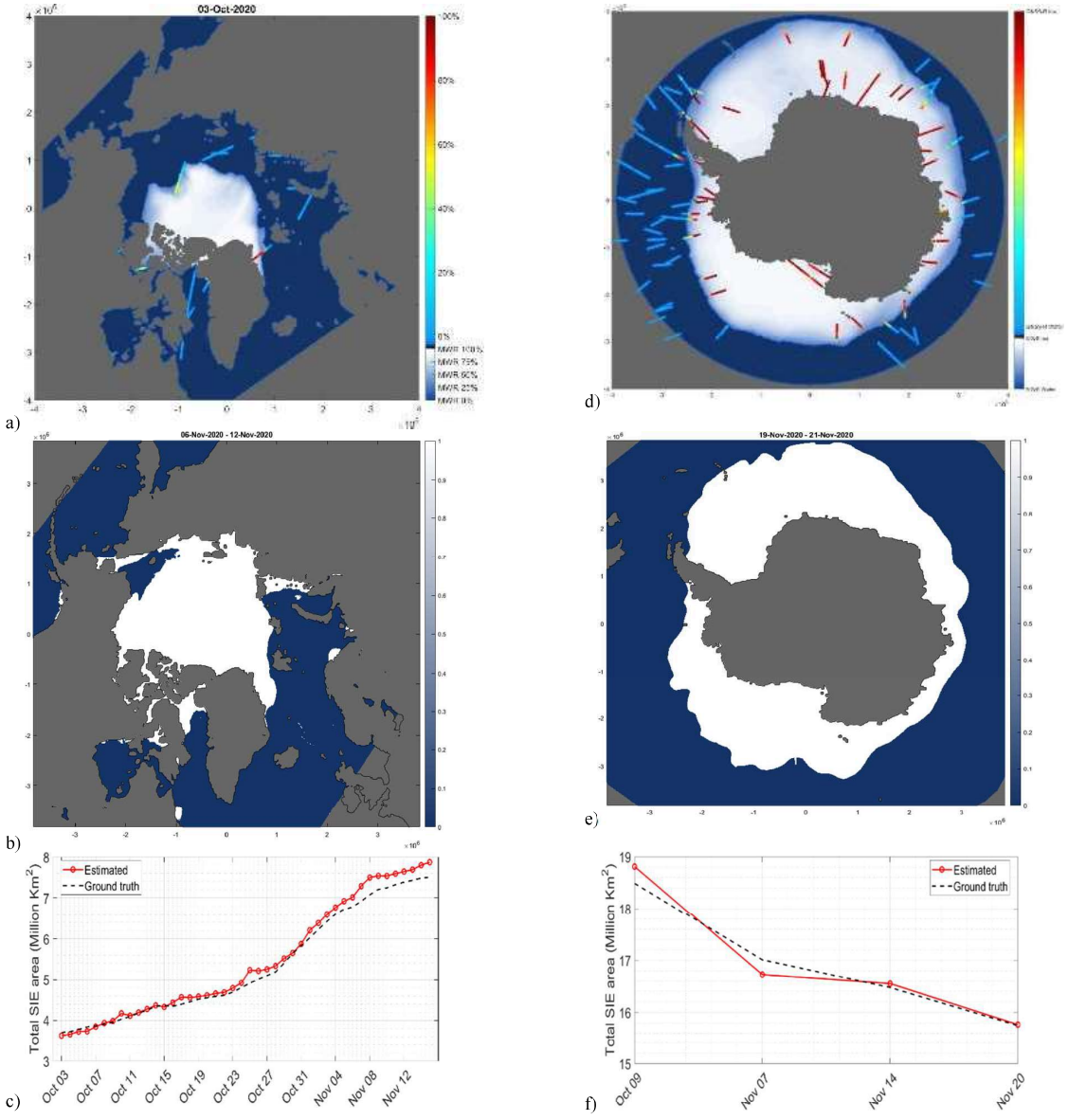

Fig. 4. Sample SIE (top) and SIC (center) maps for the Arctic and Antarctica, as derived from FMPL-2, and (bottom) temporal evolution during October and November. Error is < 6% when compared to OSI SAF "ground truth" (adapted from [12]).

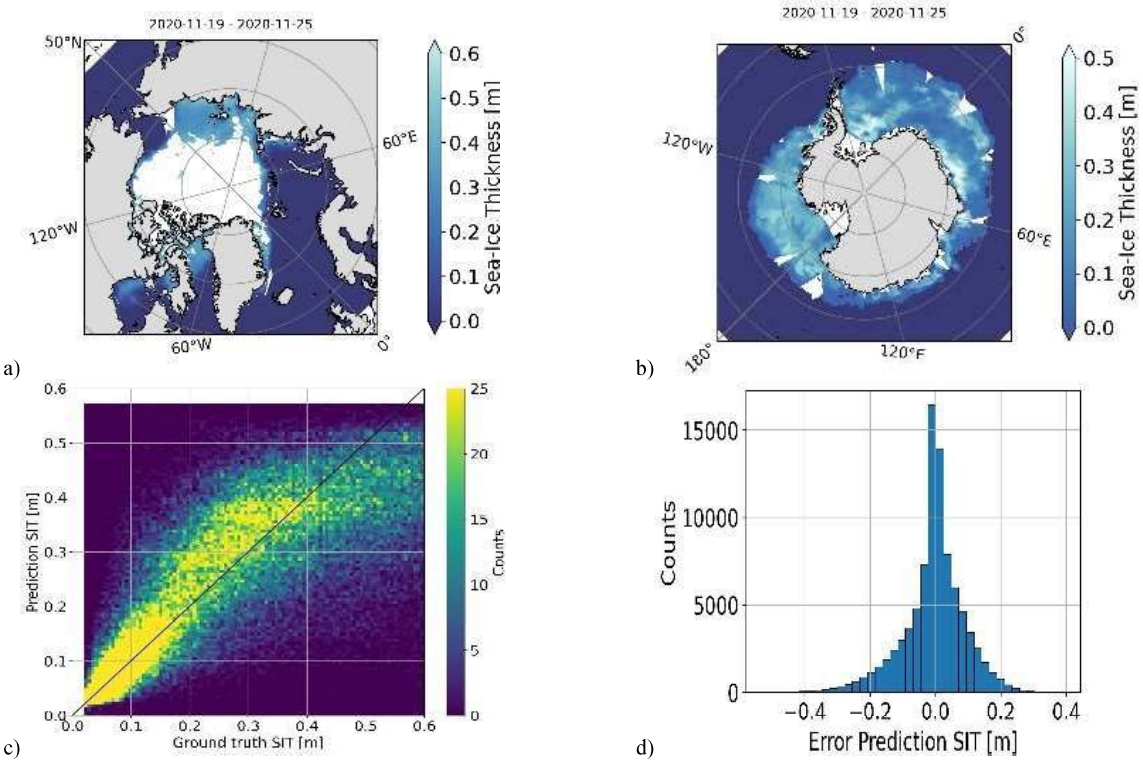

Fig. 5. Sample SIT maps over a) the Arctic, b) Antarctica, and error statistics: c) SMOS SIT ground truth/FMPL-2 DNN SIT scatter plot, and d) MAE histogram (from [12]).

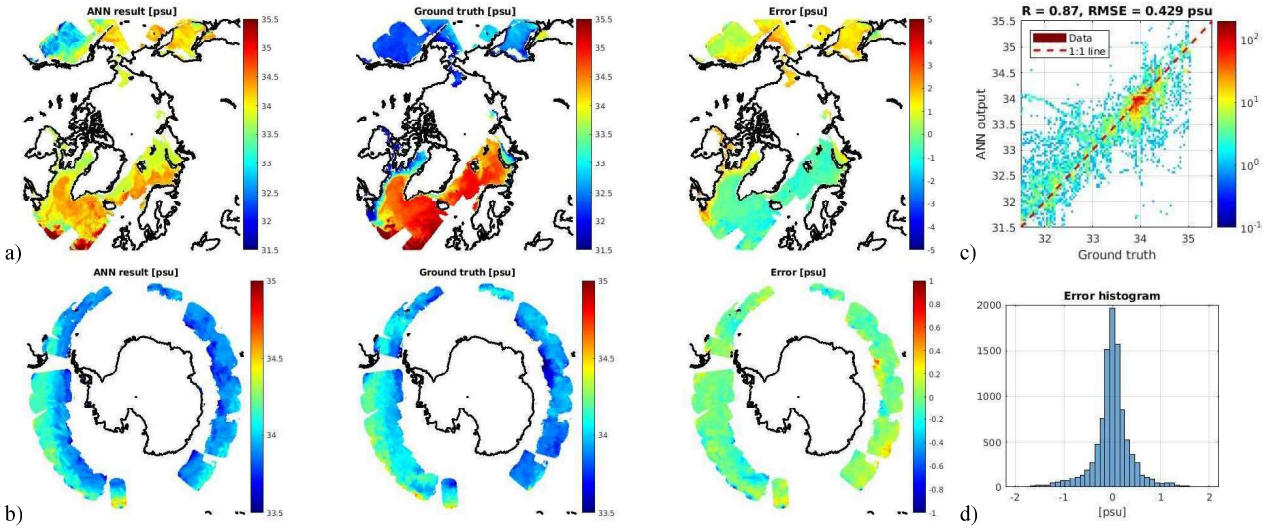

Fig. 6. Sample retrieved, ground truth, and SSS error maps over a) the Arctic, b) Antarctica, and error statistics: c) SMOS SSS ground truth/FMPL-2 ANN SSS scatter plot, and d) MAE histogram (from [14])